#### **RESEARCH**



# Neuromorphic properties of flexible carbon nanotube/polydimethylsiloxane nanocomposites

Ruochen Liu<sup>1</sup> · Jae Gwang Kim<sup>1</sup> · Prashant Dhakal<sup>2</sup> · Wei Li<sup>2</sup> · Jun Ma<sup>3</sup> · Aolin Hou<sup>1</sup> · Cory Merkel<sup>4</sup> · Jingjing Qiu<sup>5</sup> · Mark Zoran<sup>6</sup> · Shiren Wang<sup>1,2,3</sup>

Received: 17 August 2022 / Revised: 17 November 2022 / Accepted: 3 December 2022 © The Author(s), under exclusive licence to Springer Nature Switzerland AG 2022

#### **Abstract**

Neuromorphic materials are promising for fabricating artificial synapses for flexible electronics, but they are usually expensive and lack a good combination of electronic and mechanical properties. In this paper, low-cost flexible carbon nanotube/polydimethylsiloxane (CNT/PDMS) nanocomposites were prepared by solution processing. Their neuromorphic properties were studied as a function of PDMS macromolecular network structure. Specifically, the structural defects of the polymer network originating from intermolecular crosslinking reactions were tuned to tailor the electron transfer between carbon nanotubes, resulting in a recorded low switching power consumption  $(1.40 \times 10^{-10} \text{ W})$  and a high working bending radius of curvature (5 mm) compared to other organic, flexible neuromorphic materials. As-fabricated CNT/PDMS composites demonstrate robust performance for  $10^4$  operating cycles under mechanical deformation. Emulation of synaptic functions was also presented, showing long-term potentiation (LTP) and long-term depression (LTD) characteristics. These results lay a foundation for networked polymer-based multifunctional nanocomposites for flexible neuromorphic electronic devices.

Keywords Neuromorphic materials · Artificial synapse · Carbon nanotubes · Memristor · Nanocomposite

## 1 Introduction

The need for multifunctional composites is growing due to their synergistic functions suitable for increasingly complex application scenarios [1–3]. Recent advances in flexible and

Ruochen Liu, Jae Gwang Kim, and Prashant Dhakal equally contributed to this work.

- Shiren Wang s.wang@tamu.edu
- Department of Materials Science and Engineering, Texas A&M University, College Station, TX 77843, USA
- Department of Industrial and Systems Engineering, Texas A&M University, College Station, TX 77843, USA
- Department of Biomedical Engineering, Texas A&M University, College Station, TX 77843, USA
- Department of Computer Engineering, Rochester Institute of Technology, Rochester, NY 14623, USA
- Department Mechanical Engineering, Texas A&M University, College Station, TX 77843, USA

Published online: 17 December 2022

Department of Biology, Institute of Neuroscience, Texas A&M University, College Station, TX 77843, USA

wearable electronics drive the development of multifunctional composites that combine good electronic and mechanical performances. Upon deployment, it is imperative that the massive amount of data generated by electronic devices can be stored and processed efficiently. Memristor-based artificial synapses are promising for energy-efficiency neuromorphic computing. Particularly, nanocomposite materials having nanoscale fillers embedded in organic matrices are promising for flexible neuromorphic electronics due to their mechanical flexibility, biocompatibility, and simple fabrication process [3–5]. Also, low energy consumption for flexible memristor units has been sought after because it is critical for densely packed data analysis [5–9]. Several attempts to achieve high energy efficiency against mechanical deformation were based on incorporating natural materials [10–12], which could achieve  $1.50 \times 10^{-10}$  W resistive switching power consumption with a working bending radius of curvature of 15 mm. Although natural materials have been widely explored for flexible memristive devices, they could lack diversity for structural customization [13] or require additional chemical modification to exhibit neuromorphic behaviors. For example, it would take weeks to harvest protein nanowires from the bacterium Geobacter



sulfurreducens in a strictly controlled environment to fabricate a protein–nanowire film-based active layer [14, 15].

On the other hand, synthetic polymers like polydimethylsiloxane (PDMS) and silicon elastomers are cheap, ready to use, flexible, and biocompatible, which is a promising candidate for flexible organic matrices for nanocomposite electronics [16]. The molecular structure of PDMS is also easily tuned for many applications, but its nature of nonconductive property hindered its neuromorphic application. Incorporating conductive fillers, such as carbon nanotubes, into polymer nanocomposite materials is promising to overcome this problem. Single-wall carbon nanotubes (SWCNT) are widely used in electronics due to their exceptional conductivity and high aspect ratio. A small amount of inclusion can significantly improve the electrical properties of the non-conductive polymer matrix [17, 18]. However, the neuromorphic properties of flexible SWCNT/PDMS nanocomposites remain unknown. Although the macromolecular structure influences the mechanical and thermal properties of materials in various applications [19-22] and electrical sensing and conducting behavior are well-studied [23], its effects on memristive behavior have not been studied.

In this paper, PDMS/SWCNT nanocomposites were prepared by simple solution processing with an extra low loading of SWCNT, and their neuromorphic functionalities were studied. By tuning the PDMS crosslinking density, the resultant memristor's operation voltage can be adjusted as low as 0.7 V, and a switching power consumption of  $1.40\times10^{-10}$  W with a high bending radius of curvature of 5 mm. The memristive performance also demonstrated good stability against cyclic switching and the ability to mimic the biological synapse behavior.

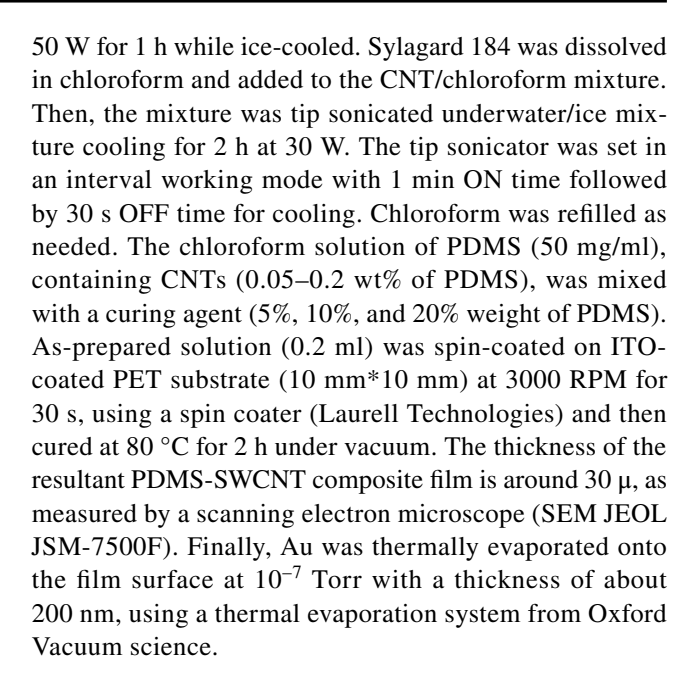
## 2 Experimental

#### 2.1 Materials

The single-wall carbon nanotube (SWCNT) was purchased from Raymor Industries. The SWCNT's outer diameter, length, and density were 1.2–1.7 nm, 100–4000 nm, and 1.3 g cm<sup>-3</sup>, respectively. Silicon elastomer base and curing agent (Sylgard 184) was purchased from Dow Corning. ITO-coated PET was purchased from Adafruit. Chloroform (MACRON Chemicals) and DMF (Sigma-Aldrich) were used as received.

#### 2.2 Device fabrication

The scheme of nanocomposite memristor fabrication is shown in Fig. 1. SWCNTs were ground with mortar and pestle with 4–5 drops of DMF into a black paste state. The paste was mixed with chloroform and tip-sonicated at



### 2.3 Device characterization

Crosslinking density was determined using a solvent-swelling method according to the literature, and the calculation is given as follows [20]:

$$v_e = \frac{\left[ln(1 - V_2) + V_2 + \chi V_2^2\right]}{V_1\left(V_2^{\frac{1}{3}} - \frac{V_2}{2}\right)}$$
(1)

where  $V_1$  is the molar volume of solvent (chloroform; 80.2 ml mol<sup>-1</sup>),  $V_2$  is the volume fraction of polymer in the swollen network, and  $\gamma$  is the Flory–Huggins interaction parameter between the PDMS and chloroform. The electrical properties of devices were characterized under ambient conditions, using a Keithley 2400 SMU and 4200 PMU. The characteristic I-V curve was measured by voltage sweep (170 mV/s). Currents at LRS and HRS were obtained at 0.2 V, 1 ms reading pulse followed by pulse voltage input, 5 V for writing, and -5 V, 1 ms pulse for erasing. PPF was characterized by sequential pulse voltage input (5 V, 1 ms width) with various time intervals ( $\Delta t$ ) from 1 to 10 ms. Long-term synaptic functions of devices were measured after  $\pm 1 \text{ V}, \pm 4 \text{ V}$ , and  $\pm 5 \text{ V}$  pulse voltage input. The sweeping rate's effect on I-V curves is performed with sweeping rates of 170 mV/s, 175 mV/s, and 180 mV/s.

## 3 Results and discussion

The design of the neuromorphic composite is inspired by the structure of the synapse, where signals were transmitted from presynaptic axons to postsynaptic dendrites through a



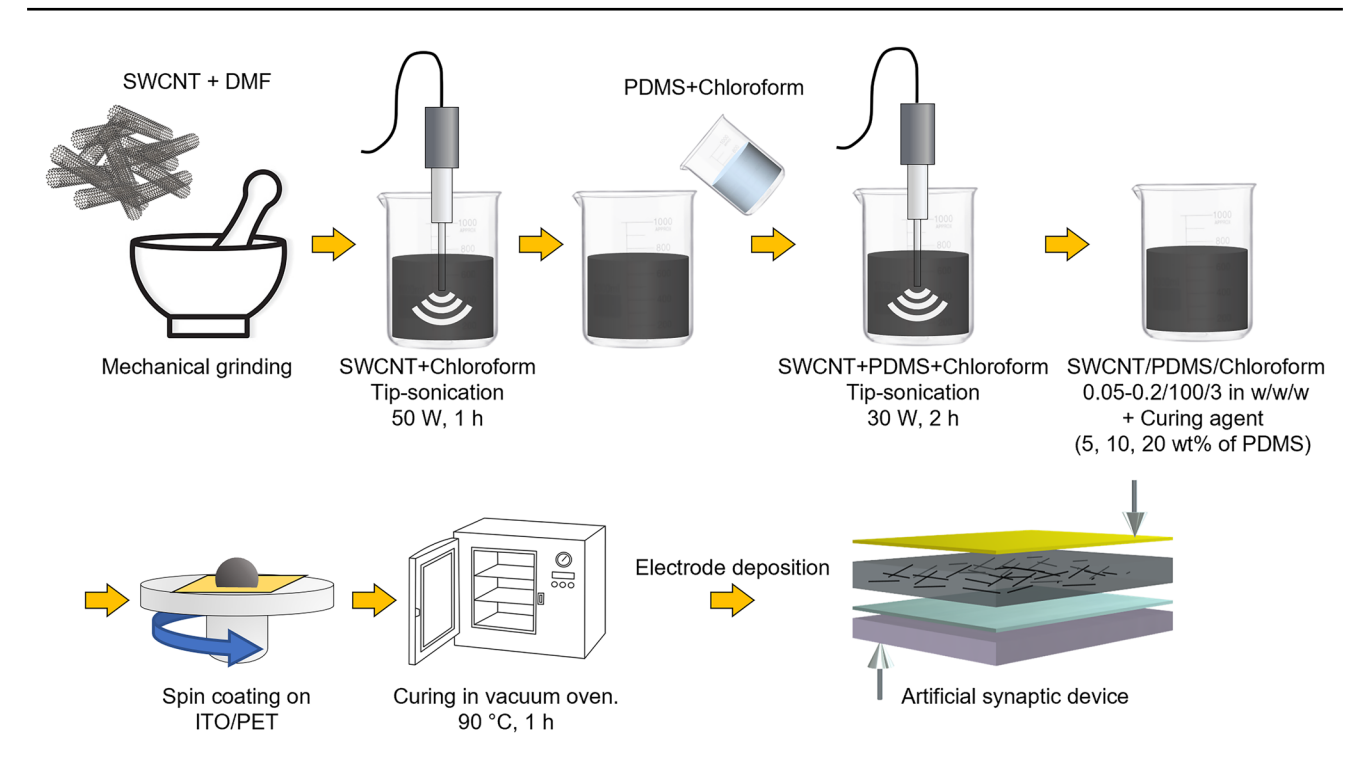


Fig. 1 Schematic description for the fabrication of flexible carbon nanotube/ polydimethylsiloxane nanocomposite memristor

synaptic cleft (Fig. 2a). The sandwich-structured composite consists of a bottom electrode (BE), an active middle layer, and a top electrode (TE) to simulate the synapse function, as illustrated in Fig. 2b. A commercially available flexible electrode, indium tin oxide (ITO)-patterned polyethylene terephthalate (PET) membrane, was used as the bottom electrode. The ITO/PET as BE is commercially available and lowcost, offering flexibility and an excellent interface for BE and PDMS-based middle layers [24]. SWCNT dispersed in PDMS was spin-coated on ITO/PET BE with 20-µm thickness, which serves as an active middle layer for non-volatile bipolar resistive switching behavior (Fig. 2c). The dispersed size of SWCNT in the PDMS active layer was examined by an atomic force microscope (AFM), as shown in Fig. 2d.

SWCNTs were dispersed in the PDMS matrix as exploited small bundle, with a small loading of 0.1 wt% concentration to achieve highly efficient charge transportation. The SWCNTs' concentration affects the devices' electrical performance, as shown in Fig. S1. Due to the insulating nature of pure PDMS, the low SWCNT concentration (0.01 wt%) device exhibited only an insulating state (Fig. S1a). On the other hand, the device's current–voltage (I-V) characteristics with 0.1 wt% CNT content displayed resistive switching behavior (Fig. S1b). The 0.1 wt% of SWCNT content is theoretically the upper limit of possible resistive switching because the percolation threshold of SWCNT (d=1.2-1.7 nm, l=100-4000 nm,  $\rho=1.3$  g cm<sup>-3</sup>) is about 0.1 wt% as calculated by the following equation [25]:

$$\phi_c = \frac{V_{\text{rod}}}{V_{\text{ex}}} = \frac{\frac{\pi}{4}d^2l}{\frac{\pi}{2}d\left(\frac{\pi}{4}d^2 + l^2\right) + \frac{\pi}{4}d^2l(3+\pi)}$$
(2)

The theoretical percolation threshold and experiment variance are because SWCNTs are slightly aligned in the shear field during the spin coating process with 2000-RPM speed, where the resultant theoretical threshold was 0.065–0.097 wt%. In high SWCNT loading (0.2 wt%), the device exhibited conductive behavior with SWCNTs forming conducting paths with a percolated network (Fig. S1c). Au was deposited as the top electrode by thermal evaporation with a thickness of around 100 nm, as shown in Fig. 1c. The matrix material of the middle layer of Au/CNT-PDMS/ITO devices was fabricated with 5: 1, 10: 1, and 20: 1 elastomer/curing agent ratio to investigate the polymer structure effect on the electrical performance, which was named device A (5: 1), device B (10: 1), and device C (20: 1), respectively.

Vertically assembled sandwich-structured devices exhibit bipolar resistive switching behavior with continuous voltage sweep experiments at a rate of 170 mV s<sup>-1</sup>, under an ambient environment (Fig. 3a–c). The electrical performance of fabricated memristors was characterized using a Keithley 2400 SMU semiconductor analyzer. In a representative voltage sweep loop, the devices exhibited bipolar resistive changing behavior, the transition from the high resistance state (HRS) to the low resistance state (LRS) at each turnon voltage ( $V_{\rm on}$ ). At 0 V, device A demonstrated an HRS



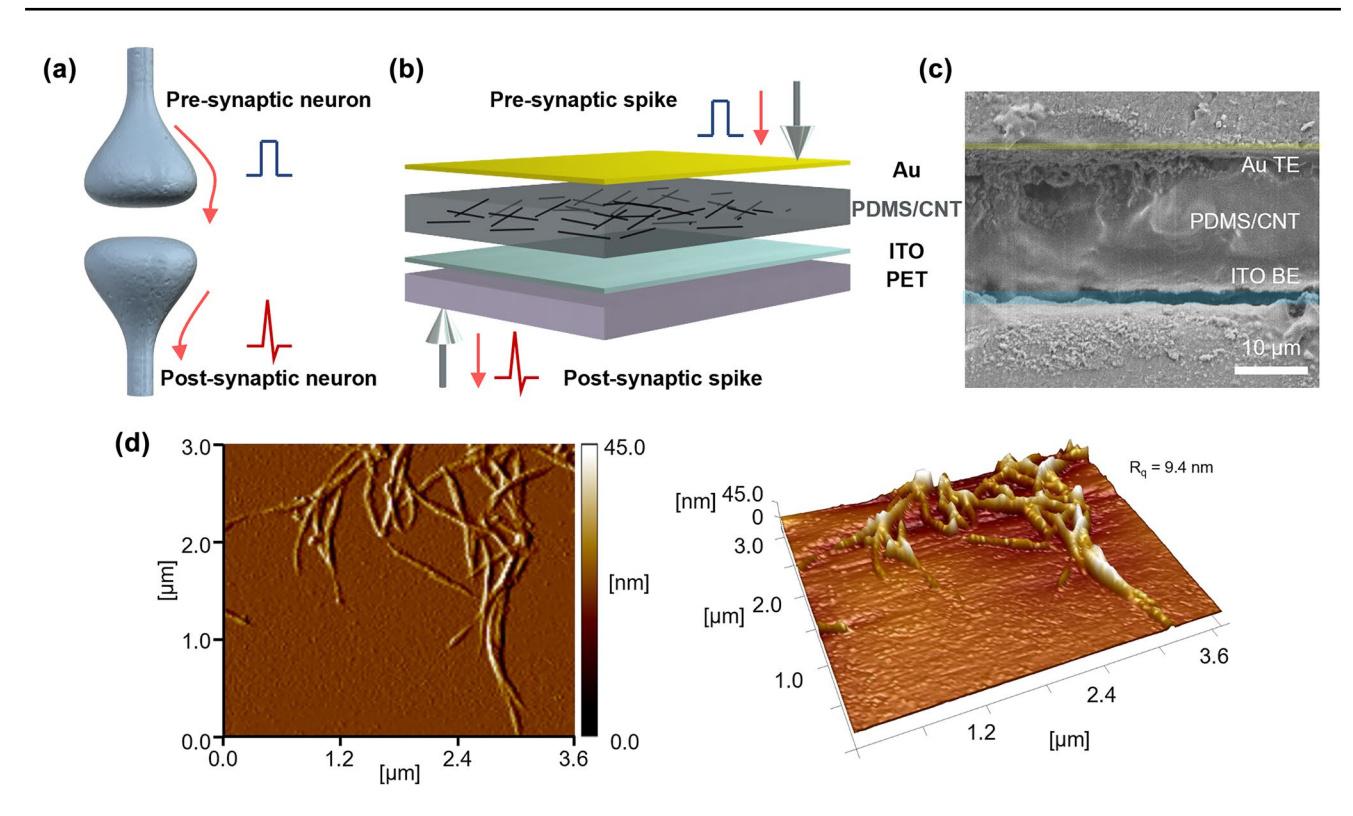


**Fig. 2** Structure of the composite memristor device. (a) Illustration of the structure of a synapse. (b) Illustration of the architecture of SWCNT/PDMS nanocomposite memristor with Au top electrode, ITO bottom electrode, and PET substrate to simulate the neuromorphic

function. (c) Cross-sectional SEM image of the SWCNT/PDMS nanocomposite memristor with a 10- $\mu m$  scale bar. (d) AFM images of well-dispersed 0.1 wt% CNT-PDMS active layer with root-mean-square roughness of 9.4 nm

until the voltage of  $4.4 \pm 0.3$  V ( $\pm$  standard deviation) was applied. The current curve experienced a spiking increase of up to three times magnitude, indicating a conductivity transition from the HRS to the LRS. When exceeding the  $V_{\rm on}$ , device A stayed in LRS. The LRS state was retained at reversing voltage sweep until it was switched off at a turn-off voltage  $(V_{\text{off}})$  of  $-4.3 \pm 0.3$  V (Fig. 3a). The device then remained in the HRS until the next voltage sweeping, after which the cycle was repeated. Also, device B switched from HRS to LRS at  $3.2 \pm 0.4$  V ( $V_{on}$ ) and LRS to HRS at  $-3.8 \pm 0.1$  V ( $V_{\rm off}$ ), as illustrated in Fig. 3b. Most importantly, device C demonstrated  $V_{\rm on}$  at  $0.6 \pm 0.01~{\rm V}$ and  $V_{\rm off}$  at  $-0.7 \pm 0.5$  V (Fig. 3c), decreasing crosslinking density of active layer from  $(7.3 \pm 0.9) \times 10^{-3}$  mol cm<sup>-3</sup> (device A) to  $(4.4 \pm 1.1) \times 10^{-3}$  mol cm<sup>-3</sup> (device B) and  $(1.95 \pm 0.32) \times 10^{-3}$  mol cm<sup>-3</sup> (device C) (Fig. 3d) leads gradual reducing of both  $V_{\rm on}$  and  $V_{\rm off}$  of all devices from 4.7 V to 0.7 V (Fig. 3e). Despite the SWCNT content being the same at all devices, the difference in switching voltage indicated that the structure of the PDMS matrix affects the transport phenomena of electrons between the SWCNTs under external electrical fields.

The exceptional ON/OFF tunability can be attributed to the crosslinking density-controlled charge trapping dynamics at the

functional composite middle layer of the device. We attribute the operation mechanism of the resistive switching to the trapcontrolled charge transport, which is illustrated in Fig. 4a and b. The HRS was stabilized by the selective electron trap in a space-charged layer between SWCNTs and PDMS matrix with a superficial level. After reaching a threshold during the first 0 to 5 V sweep, the electrons trapped in SWCNT were selectively released at a specific positive voltage  $(V_{on})$  under the applied electronic field. As a result, the device switched from HRS to the fully charged LRS, where trapped electrons freely flow. In the last cycle, the device switched from the LRS to the HRS at  $V_{\rm off}$ , where all the electrons trapped in the spacecharged layer were fully released. As a result, the device returns to the low conductivity state (Fig. 4d-f). Along this mechanism, the decreases in the On and Off voltage of the devices from 4.7 V to 0.7 V (Fig. 3e) can be attributed to the different electrical properties of PDMS, which is related to crosslinking density; the lower activation energy for effective charge carrier hopping and thus a reduced threshold switching voltage. Based on the dielectric layers sandwiched between the electrodes, the resistive switching behavior has been explained with different mechanisms. To study the resistive switching mechanism in our system, the I-V curves have been fitted with the trap-controlled surface-charge limited conduction (SCLC)



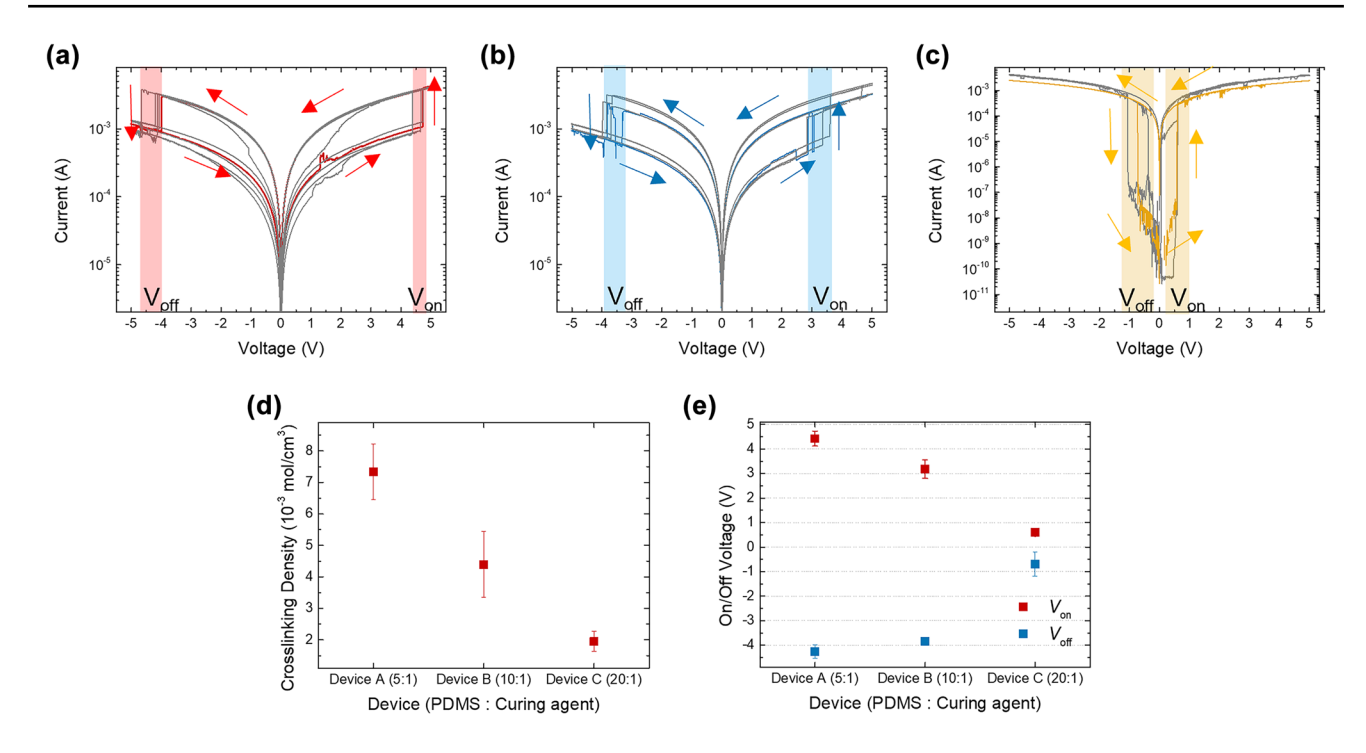


**Fig. 3** Molecular structure dependence of the resistive switching behavior. Current–voltage (I-V) curves under 5 voltage sweep cycles of (a) device A, (b) device B, and (c) device C. Arrow indicates the voltage sweep path. (d) Crosslinking density of devices with differ-

ent mixing ratios. (e) Molecular structure dependence of On and Off voltages, 5:1 for device A, 10:1 for device B, and 20:1 for device C (PDMS: curing agent ratio)

mechanism, which is controlled by defects [26]. In our system, the structural defects were related to the following mechanism for forming the conduction path between carbon nanotubes. As well-known polymer chemistry, PDMS undergoes an intermolecular crosslinking reaction with a curing agent, controlling the crosslinking density by varying the curing agent. Consequently, a highly crosslinked polymer network has fewer structural defects (dangling ends, unreacted sites) than a loosely crosslinked polymer network with more structural defects. As illustrated in Fig. 4b and c, higher defect concentration due to lower crosslink density leads to a lower threshold voltage to transport electrons in the space-charged layer between SWCNTs and PDMS matrix across the polymer networks; the structural defects make additional energy states ( $E_{\text{defect}}$ ) below the original energy barrier level of PDMS (Fig. 4c, S3) which enable electrons trapped on the CNT-PDMS interfaces moves to the next trap (CNT) easier than no-defect condition (fully crosslinked); the low charge carrier mobility in networked structure and crystalline regions leads the lower conductivity of highly crosslinked polymer than less crosslinked, linear, and amorphous polymer matrix [27].

The I-V curves of the devices are illustrated in a double-logarithmic scale, as shown in Fig. 4d–f, to verify the SCLC model in our system. The I-V curve characteristic of trap-controlled consists of three parts in HRS: (1) Ohmic region  $(I \propto V)$  observed at low bias, (2) shallow trap SCLC  $(I \propto V^n)$ ,

(3) trap-filled-limit SCLC, and (4) trap-free SCLC that steep current increase observed at the high electrical field, especially over the threshold voltage ( $V_{\rm on}$ ). The I-V curves are matched with the trap-controlled SCLC mechanism. In particular, at low voltage, the current conduction follows Ohm's law with a slope of 1. At higher voltage (Fig. 4f), the shallow trap SCLC mechanism could be dominant. During this intermediate region, the charge transport is regulated by trapping and de-trapping of the charge carrier. The current–voltage relationship follows the Mark–Helfrich law[28] where the trapped are exponentially distributed (Figure S2) and follows the equation below:

$$J_{\text{exp}}(V,T) = N_0 \mu e^{1-l} \left( \frac{\varepsilon}{N_{\text{trap}}} \frac{l}{l+1} \right)^l \left( \frac{2l+1}{l+1} \right)^{l+1} \frac{V^{l+1}}{d^{2l+1}}$$
 (3)

where  $N_0$  is the effective density of states at the conduction band edge,  $\mu$  is the mobility of charge carriers,  $\varepsilon$  is the permittivity of the composite film,  $N_{\rm trap}$  is the trap density, l is the power coefficient, and l>1, v is the effective voltage, and d is the thickness of the composite film. It can be obtained that in this region,  $I \propto V^n$  and n>2 according to Eq. (3). Figure 3d–f shows a typical transition of the current–voltage scaling from low-bias Ohmic regime trap-filled limited SCLC and the recovery of the trap-free regime at high bias, suggesting that the trap-controlled SCLC controls the switching mechanism.



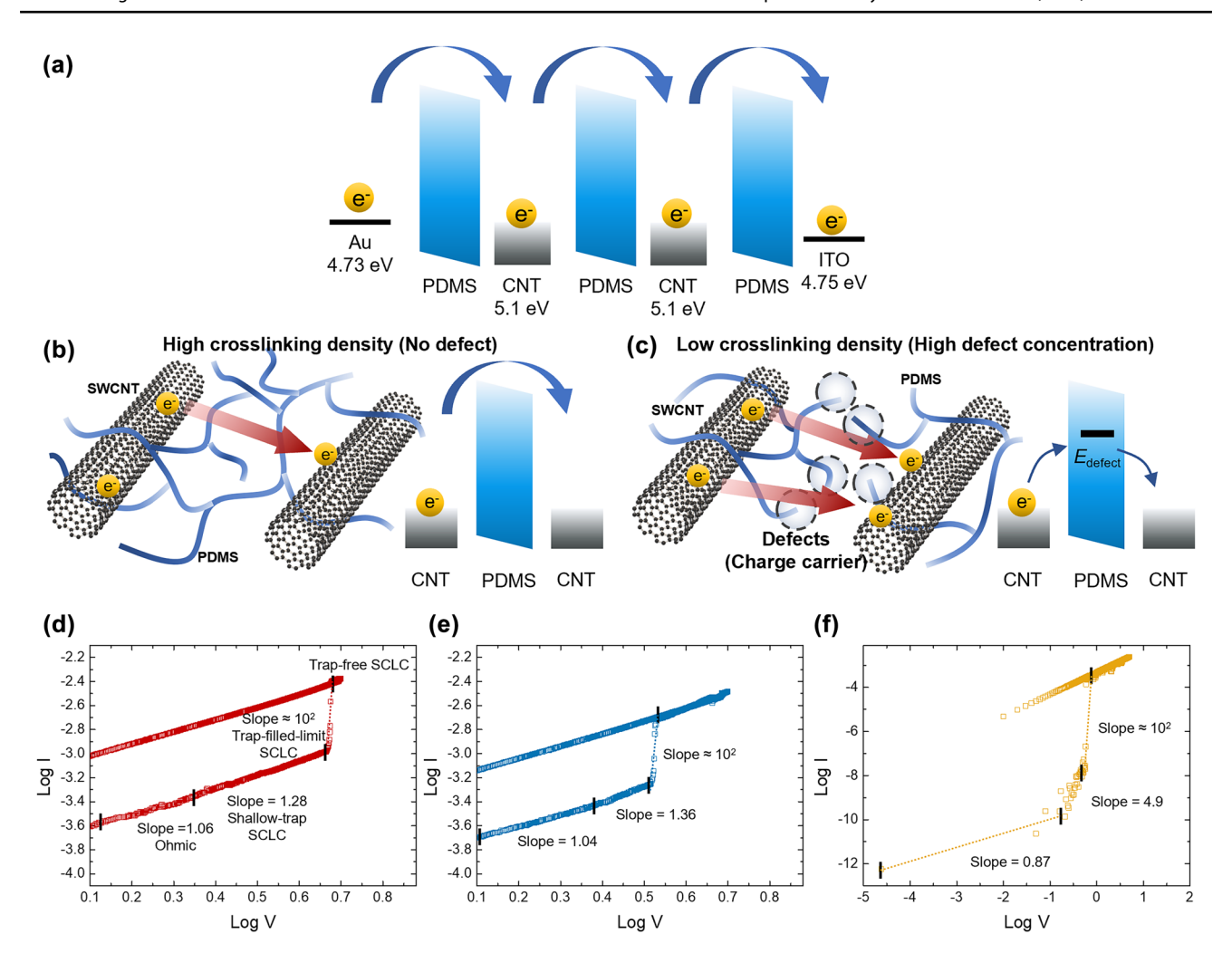


**Fig. 4** Operation mechanism of resistive switching devices. (**a**) Schematic energy diagram and charge transportation of resistive switching devices. (**b**, **c**) Molecular structure-dependent space-charge limited conduction mechanism of PDMS/SWCNT nanocomposite memristor in (**b**) high crosslinking density and (**c**) low crosslinking density.

Double logarithm plot of I-V curves of ( $\mathbf{d}$ ) device A, ( $\mathbf{e}$ ) device B, and ( $\mathbf{f}$ ) device C for scaling transitions from the low-bias Ohmic curve regime, shallow-trap SCLC, trap-filled limit SCLC, and trap-free SCLC at high voltage

The slope value in the trap-controlled region (n = 4.9) in low crosslinking density device C supports the shallow trap SCLC mechanism suggesting that high-density structural defects (free ends, dangling ends) help electron transport. They could also form a physical hopping path via local change of conformational alignment along the applied electronic field. In addition, we noticed the sweeping rate dependence of resistive switching behavior (Fig. S3), which can also be attributed to the SCLC-controlled switching mechanism, where the transition from SCLC to Ohmic conduction as the sweeping rate increases.

The electronic performances are tested to demonstrate the potential of our device to serve in flexible electronic applications. Stability against voltage stress is essential for electrical performance of resistive switching devices. The cyclic stability of Au/CNT-PDMS/ITO devices with different crosslinking densities was developed by measuring the current at the On state  $(I_{on})$  and Off state  $(I_{off})$ with the eclipse of cycles at the reading voltage of 0.2 V after each writing voltage of 5 V and erasing voltage of -5 V (Fig. S4) up to  $10^4$  times (Fig. 5) under ambient condition. Device A was stable for 10<sup>4</sup> cycles, and device B was also steady with no visible degradation of the On/Off ratio (Fig. 5a and c). Also, the  $I_{\rm on}$  of device C, a low crosslinking density device (20:1), was maintained for  $10^4$  cycles. The statistical distributions of  $I_{\rm on}/I_{\rm off}$ and log-normal relevant results (Fig. 5b, d, and f) indicate the average values of  $I_{on}$  increase from  $0.985 \pm 0.019 \, \mu A$ (device A) to  $1.075 \pm 0.018 \,\mu\text{A}$  (device B) and finally reach  $1.159 \pm 0.028 \mu A$  (device C) as crosslinking density decreases, with the ratio of current at each HRS and LRS  $(I_{on}/I_{off})$  increases from 2.62 for device A to 2.67 for



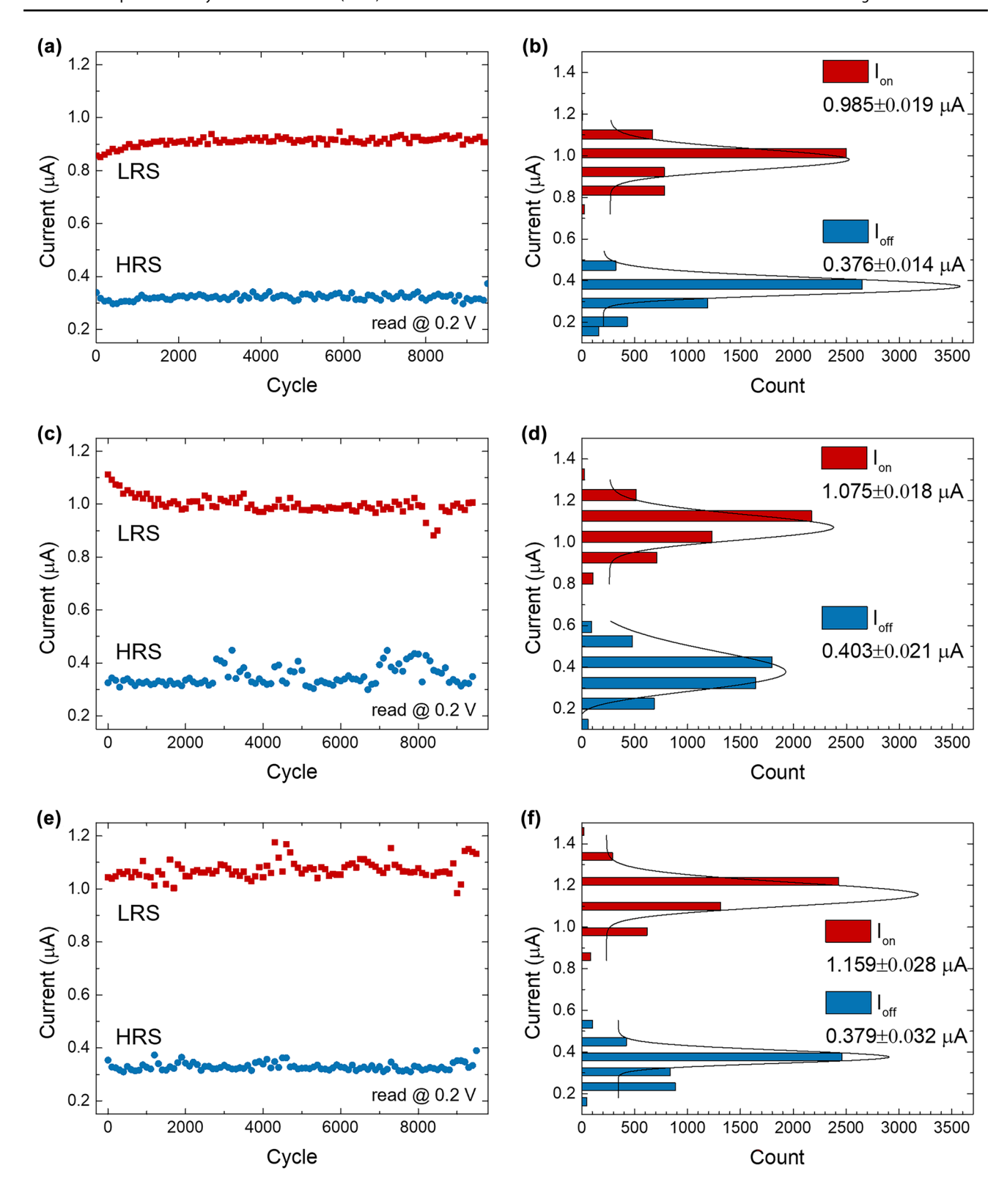
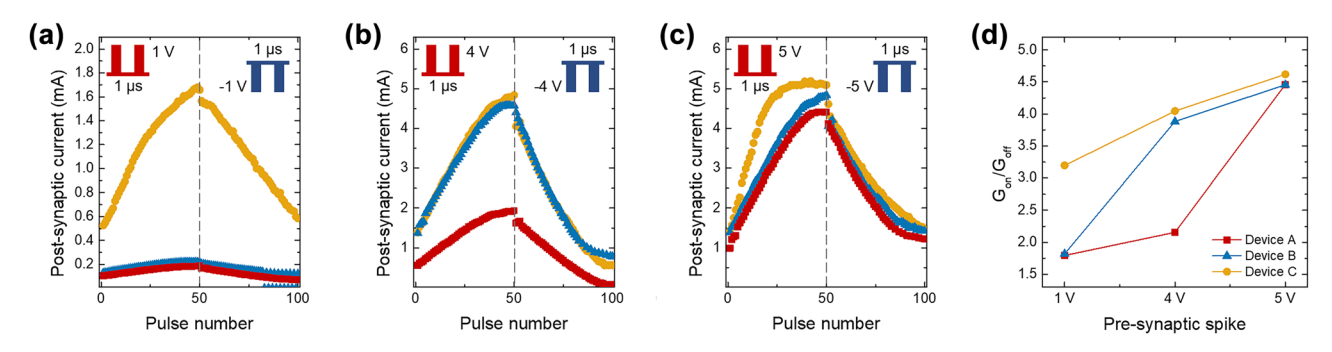


Fig. 5 The cyclic stability of the nanocomposite memristor and histogram of currents at On and Off states with different crosslinking densities. Device A (a, b), device B (c, d), and device C (e, f). The black lines are log-normal fits to the distributions





**Fig. 6** The long-term potentiation (LTP) and long-term depression (LTD) of artificial synaptic devices with various pre-synaptic pulse amplitudes ( $\blacksquare$ : device A,  $\blacktriangle$ : device B, and  $\blacksquare$ : device C). Presynaptic pulse with 1 ms width and 1 ms time interval ( $\Delta t$ ) with ( $\mathbf{a}$ )  $\pm$  1 V,

(b)  $\pm 4$  V (b), and (c)  $\pm 5$  V amplitude (positive for potentiation and negative for depression). (d) The conductance On/Off ratio ( $G_{\rm on}/G_{\rm off}$ ) corresponds to the pre-synaptic spike amplitude for the devices with different crosslinking densities

device B and finally 3.06 for device C. The higher ratio between  $I_{\rm on}/I_{\rm off}$  promises a low misreading rate and high device accuracy during operation. Thus, device C provides the best electrical performance.

Furthermore, the emulation of synaptic behaviors is critical functionality for the artificial counterparts to be used in neuromorphic devices. Here, we demonstrated that our multifunctional nanocomposite could also mimic the

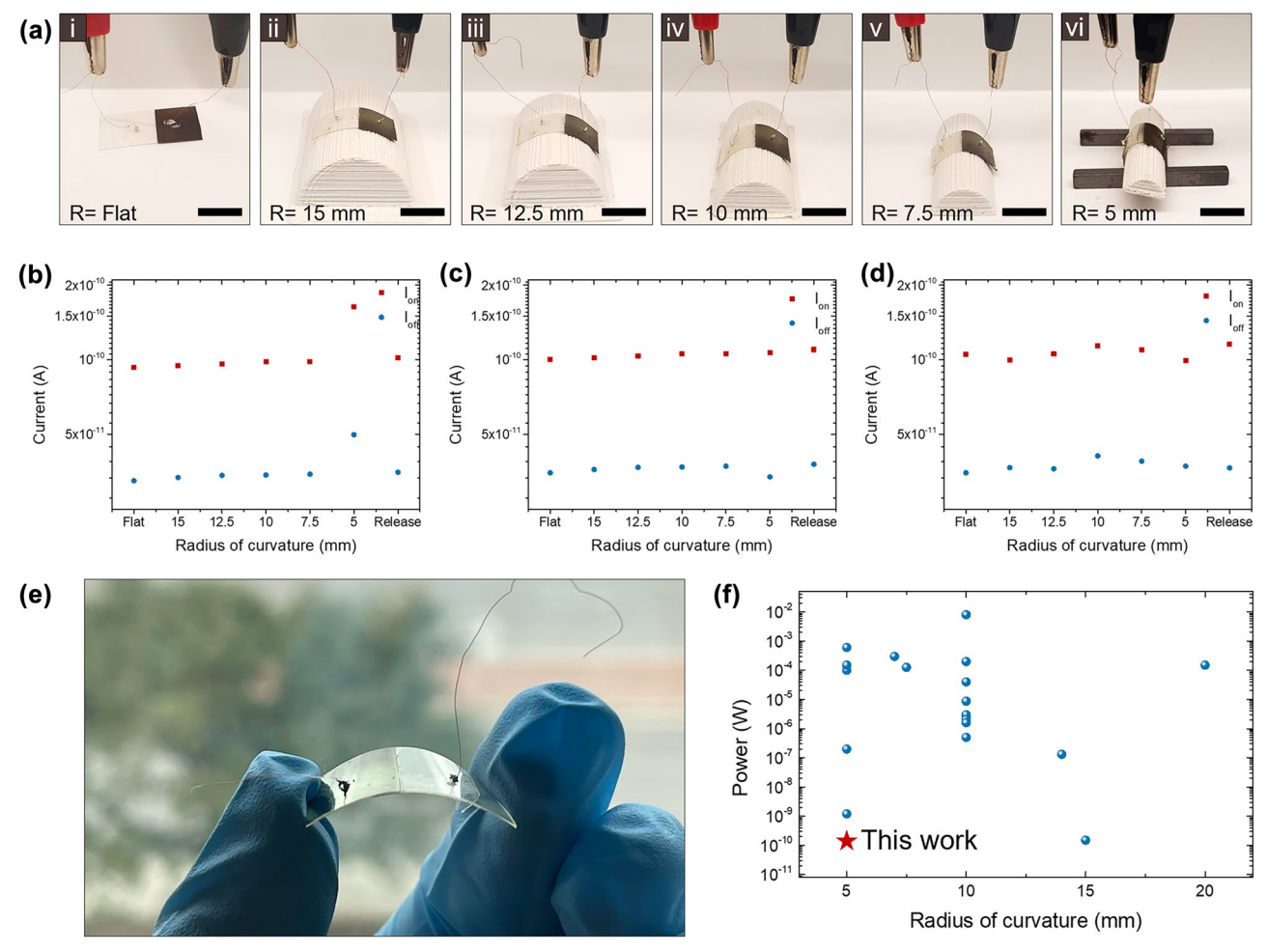


**Fig. 7** The performance of flexible memristor under bending deformation. (a) Sequential electrical measurement for the flexible device under different radii of curvature (R) from flat (i) to 15(ii), 12.5 (iii), 10 (iv), 7.5 (v), 5 (vi) mm, respectively, with 10 mm scale bar. (**b**-**d**) Current at On state ( $I_{on}$ ) and Off state ( $I_{onf}$ ) of (**b**) device A, (**c**) device

B, and (d) device C under flexural deformation. (e) The photograph image of the mechanical flexibility of the device. (f) The power consumption versus minimum radius of curvature of flexible memristors [11, 29–46]. For data, see table S1



synaptic functions of long-term potentiation (LTP) and depression (LTD), which are essential for constructing the artificial synaptic device. In detail, LTP/LTD represents temporal or long-lasting enhancement or decaying of synaptic connections related to long-term memory. The synaptic functions of SWCNT-PDMS devices are measured by the Keithley 4200A-SCS parameter analyzer shown in Fig. 6 to mimic the biological synapses. A model of longterm memorization and forgetting of the artificial synapse was demonstrated by using a pulse input at three different amplitude levels (1 V, 4 V, and 5 V) between the threshold voltage  $(V_{on}; V_A, V_B, V_C)$  of each device  $(V_C < 1 \text{ V} < V_B)$  $< 4 \text{ V} < V_A < 5 \text{ V}$ ) as shown in Fig. 6a–c. For long-term potentiation (LTP), the pulse signals of 1 ms width and 1 ms time interval ( $\Delta t$ ) with different pulse amplitude (1 V, 4 V, and 5 V) were applied to devices. For long-term depression (LTD), negative pulse signals (1 V, 4 V, and 5 V) were used. Synaptic weight was enhanced after positive pre-synaptic signs and decaying with negative inputs, showing a typical LTP/LTD behavior. The low crosslinking density device C has a lower programming voltage of 1 V while obtaining the sufficient conductance ratio of On and Off states  $(G_{on}/G_{off})$ . At higher operation voltages, device B receives the acceptable On/Off ratio at 4 V, and all devices achieve synaptic functions (Fig. 6d). Therefore, this high On/Off ratio  $(G_{on}/G_{off})$  at low operation voltage (1 V) of a common crosslinking density device would provide a better opportunity for wearable and implantable applications.

A good combination of electrical performance and mechanical flexibility is the key to flexible electronics. To meet the demand for wearable and implantable electronic applications, the mechanical flexibility of the CNT-PDMS memristor was evaluated by bending the devices on semicylindrical molds with different radii of curvature (Fig. 7). The characteristic currents at HRS and LRS of the devices were measured from flat to bending state with a radius of curvature of R = 15, 12.5, 10, 7.5, 5 mm, respectively, and returned to a balanced state as shown in Fig. 7a. During the deformations of bending and relaxing, the currents in each bending state were kept stable (Fig. 7b-d). Irrespective of the bending deformations, the resistance between HRS and LRS of the device remained constant 3 times within 1.3% (device A), 1.5% (device B), and 4.6% (device C) changes, respectively, from a pristine flat state. The PDMS-CNT memristor thus demonstrates good electrical stability against mechanical deformation for wearable applications.

We compared the performance of the CNT-PDMS devices with other memristors on a two-dimensional space constructed with the power consumption within resistive transition and radius of curvature at maximum deformation (Fig. 7f). The device C optimized in this experiment, which performs the stable resistive switching at a radius of curvature of 5 mm, achieved a low power consumption of  $1.4 \times 10^{-10}$  W during

operation. The device's flexibility is well below the trend line, reaching relatively low operating power consumption variance compared to other flexible memristors [11, 29–46].

#### 4 Conclusion

We demonstrated a multifunctional, inexpensive PDMS-SWCNT nanocomposite with a low operation-voltage neuromorphic behavior. The resistive switching behavior of the PDMS-SWCNT nanocomposite is tuned by controlling the network structure of the PDMS matrix by varying the crosslinking density. The electron transport between disconnected SWCNTs depends on defects concentration, which is related to the crosslinking density of polymer networks. The underlying mechanism is ascribed to the space-charge limited conduction (SCLC) theory. The low threshold resistive switching voltage of 0.7 V was achieved by lowering the crosslinking density of the PDMS matrix, offering a high defect concentration. Also, the devices demonstrated successful emulation of biological synaptic properties (LTP/ LTD), which is essential for constructing artificial neural networks. The device performs high endurance (10<sup>4</sup> cycles) and flexibility. Besides, the PDMS-SWCNT nanocomposite memristors demonstrated unprecedented low operating power consumption  $(1.4 \times 10^{-10} \text{ W})$  against high mechanical deformation (5 mm radius of curvature bending) compared to reported flexible neuromorphic devices. The flexible CNT/PDMS artificial synapse device was also attractive due to the low-cost, commercially available materials. Overall, polymer network engineering provides an efficient avenue toward the multifunctional composite design of flexible neuromorphic computing devices.

**Supplementary Information** The online version contains supplementary material available at https://doi.org/10.1007/s42114-022-00599-9.

**Author contribution** S.W. conceived the research. S. W., R. L., and J. K. designed the experiments. R. L., J. K., P. D., A. H., W.L., and J. M. prepared samples and measured the properties. R. L., J. K., J. Q., C. M., M. Z., and S. W. analyzed the data and wrote the manuscript with comments and inputs from all authors.

Funding The authors appreciate the funding support from the National Science Foundation and Texas A&M President's Excellent Fund.

#### **Declarations**

Conflict of interest The authors declare that they have no conflict of interest.

## References

 Narayana KJ, Gupta Burela R (2018) A review of recent research on multifunctional composite materials and structures with their applications. Mater Today Proc 5:5580–5590. https://doi.org/10. 1016/j.matpr.2017.12.149



- 2. Ali A, Andriyana A (2020) Properties of multifunctional composite materials based on nanomaterials: a review. RSC Adv 10:16390-16403. https://doi.org/10.1039/C9RA10594H
- 3. Sun F, Lu Q, Feng S, Zhang T (2021) Flexible artificial sensory systems based on neuromorphic devices. ACS Nano 15:3875-3899. https://doi.org/10.1021/acsnano.0c10049
- 4. Lee S, Kim S, Yoo H (2021) Contribution of polymers to electronic memory devices and applications. Polymers (Basel). https:// doi.org/10.3390/polym13213774
- 5. Ghoneim MT, Hussain MM (2015) Review on physically flexible nonvolatile memory for internet of everything electronics. Electronics (Basel) 4:424–479. https://doi.org/10.3390/electronics4030424
- Wang T-Y, Meng J-L, Rao M-Y, He Z-Y, Chen L, Zhu H, Sun Q-Q, Ding S-J, Bao W-Z, Zhou P, Zhang DW (2020) Three-dimensional nanoscale flexible memristor networks with ultralow power for information transmission and processing application. Nano Lett 20:4111-4120. https://doi.org/10.1021/acs.nanolett.9b05271
- Wang T-Y, Meng J-L, Li Q-X, Chen L, Zhu H, Sun Q-Q, Ding S-J, Zhang DW (2021) Forming-free flexible memristor with multilevel storage for neuromorphic computing by full PVD technique. J Mater Sci Technol 60:21-26. https://doi.org/10.1016/j.jmst.2020.04.059
- Zhu Y, Liang J, Mathayan V, Nyberg T, Primetzhofer D, Shi X, Zhang Z (2022) High performance full-Inorganic flexible memristor with combined resistance-switching. ACS Appl Mater Interfaces 14:21173-21180. https://doi.org/10.1021/acsami.2c02264
- Zhang H, Liu R, Zhao H, Sun Z, Liu Z, He L, Li Y (2021) Research progress of biomimetic memristor flexible synapse. Coatings 12:21. https://doi.org/10.3390/coatings12010021
- 10. Fu T, Liu X, Gao H, Ward JE, Liu X, Yin B, Wang Z, Zhuo Y, Walker DJF, Joshua Yang J, Chen J, Lovley DR, Yao J (2020) Bioinspired bio-voltage memristors. Nat Commun 11:1-10. https://doi.org/10.1038/s41467-020-15759-y
- 11. Kim M-K, Lee J-S (2018) Ultralow power consumption flexible biomemristors. ACS Appl Mater Interfaces 10:10280-10286. https://doi.org/10.1021/acsami.8b01781
- 12. Ge J, Li D, Huang C, Zhao X, Qin J, Liu H, Ye W, Xu W, Liu Z, Pan S (2020) Memristive synapses with high reproducibility for flexible neuromorphic networks based on biological nanocomposites. Nanoscale 12:720-730. https://doi.org/10.1039/C9NR08001E
- 13. Austin MJ, Rosales AM (2019) Tunable biomaterials from synthetic, sequence-controlled polymers. Biomater Sci 7:490–505. https://doi.org/10.1039/C8BM01215F
- 14. Tan Y, Adhikari RY, Malvankar NS, Ward JE, Woodard TL, Nevin KP, Lovley DR (2017) Expressing the Geobacter metallireducens PilA in Geobacter sulfurreducens yields pili with exceptional conductivity. mBio 8. https://doi.org/10.1128/mBio.02203-16
- 15. Liu X, Gao H, Ward JE, Liu X, Yin B, Fu T, Chen J, Lovley DR, Yao J (2020) Power generation from ambient humidity using protein nanowires. Nature 578:550-554. https://doi.org/10.1038/ s41586-020-2010-9
- 16. Kausar A (2020) Polydimethylsiloxane-based nanocomposite: present research scenario and emergent future trends. Polym-Plast Technol Mat 59:1148-1166. https://doi.org/10.1080/25740881. 2020.1719149
- 17. Wang F, Tay TE, Sun Y, Liang W, Yang B (2019) Low-voltage and -surface energy SWCNT/poly(dimethylsiloxane) (PDMS) nanocomposite film: surface wettability for passive anti-icing and surface-skin heating for active deicing. Compos Sci Technol 184:107872. https://doi.org/10.1016/j.compscitech.2019.107872
- 18. Li Z, Nambiar S, Zheng W, Yeow JTW (2013) PDMS/singlewalled carbon nanotube composite for proton radiation shielding in space applications. Mater Lett 108:79-83. https://doi.org/10. 1016/j.matlet.2013.06.030
- 19. Flory PJ (1979) Molecular theory of rubber elasticity Polymer (Guildf) 20:1317–1320. https://doi.org/10.1016/0032-3861(79) 90268-4

- 20. Flory PJ, Rehner J (1943) Statistical mechanics of cross-linked polymer networks I. Rubberlike elasticity J Chem Phys 11:512-520. https://doi.org/10.1063/1.1723791
- 21. Bae S, Galant O, Diesendruck CE, Silberstein MN (2018) The effect of intrachain cross-linking on the thermomechanical behavior of bulk polymers assembled solely from single chain polymer nanoparticles. Macromolecules 51:7160-7168. https://doi.org/10. 1021/acs.macromol.8b01027
- 22. Kim JG, Jeon J, Sivakumar R, Lee J, Kim YH, Cho M, Youk JH, Wie JJ (2021) Light-fueled climbing of monolithic torsional soft robots via molecular engineering. Adv Intell Syst 4(3):2100148. https://doi.org/10.1002/aisy.202100148
- 23. Deng F, Zheng QS (2008) An analytical model of effective electrical conductivity of carbon nanotube composites. Appl Phys Lett. https://doi.org/10.1063/1.2857468
- Goswami S, Goswami S, Venkatesan T (2020) An organic approach to low energy memory and brain inspired electronics. Appl Phys Rev 7:21303. https://doi.org/10.1063/1.5124155
- 25. Mutiso RM, Sherrott MC, Li J, Winey KI (2012) Simulations and generalized model of the effect of filler size dispersity on electrical percolation in rod networks. Phys Rev B Condens Matter Mater Phys. https://doi.org/10.1103/PhysRevB.86.214306
- 26. Zhang P, Ang YS, Garner AL, Valfells Á, Luginsland JW, Ang LK (2021) Space-charge limited current in nanodiodes: ballistic, collisional, and dynamical effects. J Appl Phys. https://doi.org/10. 1063/5.0042355
- 27. Parodi F (1989) Physics and chemistry of microwave processing. In: Allen G, Bevington JCBT-CPS and S (eds) Comprehensive polymer science and supplements, Elsevier, Amsterdam, pp 669–728
- 28. Mark P, Helfrich W (1962) Space-charge-limited currents in organic crystals. J Appl Phys 33:205-215. https://doi.org/10. 1063/1.1728487
- Wang T, Meng J, Chen L, Zhu H, Sun Q, Ding S, Bao W, Zhang DW (2021) Flexible 3D memristor array for binary storage and multi-states neuromorphic computing applications. InfoMat 3:212-221. https://doi.org/10.1002/inf2.12158
- 30. Lee SH, Park HL, Kim MH, Kang S, Lee SD (2019) Interfacial triggering of conductive filament growth in organic flexible memristor for high reliability and uniformity. ACS Appl Mater Interfaces 11:30108-30115. https://doi.org/10.1021/acsami.9b10491
- 31. Ji X, Song L, Zhong S, Jiang Y, Lim KG, Wang C, Zhao R (2018) Biodegradable and flexible resistive memory for transient electronics. J Phys Chem C 122:16909-16915. https://doi.org/10. 1021/acs.jpcc.8b03075
- 32. Xu J, Zhao X, Wang Z, Xu H, Hu J, Ma J, Liu Y (2019) Biodegradable natural pectin-based flexible multilevel resistive switching memory for transient electronics. Small 15:1803970. https:// doi.org/10.1002/sml1.201803970
- 33. Lee S-H, Park H-L, Keum C-M, Lee I-H, Kim M-H, Lee S-D (2019) Organic flexible memristor with reduced operating voltage and high stability by interfacial control of conductive filament Growth. Phys Status Solidi – Rapid Res Lett 13:1900044. https:// doi.org/10.1002/pssr.201900044
- Hosseini NR, Lee J-S (2015) Biocompatible and flexible chitosanbased resistive switching memory with magnesium electrodes. Adv Funct Mater 25:5586–5592. https://doi.org/10.1002/adfm. 201502592
- Choi MK, Kim WK, Sung S, Wu C, Kim HW, Kim TW (2018) Flexible memristive devices based on polyimide:mica nanosheet nanocomposites with an embedded PEDOT:PSS layer. Sci Rep 8:1-8. https://doi.org/10.1038/s41598-018-30771-5
- Qian M, Pan Y, Liu F, Wang M, Shen H, He D, Wang B, Shi Y, Miao F, Wang X (2014) Tunable, ultralow-power switching in memristive devices enabled by a heterogeneous graphene-oxide interface. Adv Mater 26:3275–3281. https://doi.org/10.1002/ adma.201306028



- Zhang C, Tai YT, Shang J, Liu G, Wang KL, Hsu C, Yi X, Yang X, Xue W, Tan H, Guo S, Pan L, Li RW (2016) Synaptic plasticity and learning behaviours in flexible artificial synapse based on polymer/viologen system. J Mater Chem C Mater 4:3217–3223. https://doi.org/10.1039/c6tc00496b
- Raeis-Hosseini N, Park Y, Lee JS (2018) Flexible artificial synaptic devices based on collagen from fish protein with spike-timing-dependent plasticity. Adv Funct Mater 28:1–9. https://doi.org/10.1002/adfm.201800553
- Wu C, Kim TW, Guo T, Li F, Lee DU, Yang JJ (2017) Mimicking classical conditioning based on a single flexible memristor. Adv Mater. https://doi.org/10.1002/adma.201602890
- Le VQ, Do TH, Retamal JRD, Shao PW, Lai YH, Wu WW, He JH, Chueh YL, Chu YH (2019) Van der Waals heteroepitaxial AZO/NiO/AZO/muscovite (ANA/muscovite) transparent flexible memristor. Nano Energy 56:322–329. https://doi.org/10.1016/j. nanoen.2018.10.042
- Qian K, Tay RY, Lin MF, Chen J, Li H, Lin J, Wang J, Cai G, Nguyen VC, Teo EHT, Chen T, Lee PS (2017) Direct observation of indium conductive filaments in transparent, flexible, and transferable resistive switching memory. ACS Nano 11:1712–1718. https://doi.org/10.1021/acsnano.6b07577
- Yeom SW, You B, Cho K, Jung HY, Park J, Shin C, Ju BK, Kim JW (2017) Silver nanowire/colorless-polyimide composite electrode: application in flexible and transparent resistive switching memory. Sci Rep 7:1–9. https://doi.org/10.1038/s41598-017-03746-1

- Kim M, Choi KC (2017) Transparent and flexible resistive random access memory based on Al2O3 film with multilayer electrodes. IEEE Trans Electron Devices 64:3508–3510. https://doi.org/10. 1109/TED.2017.2716831
- Won Seo J, Park JW, Lim KS, Kang SJ, Hong YH, Yang JH, Fang L, Sung GY, Kim HK (2009) Transparent flexible resistive random access memory fabricated at room temperature. Appl Phys Lett 95:1–4. https://doi.org/10.1063/1.3242381
- Kim S, Son JH, Lee SH, You BK, Il PK, Lee HK, Byun M, Lee KJ (2014) Flexible crossbar-structured resistive memory arrays on plastic substrates via inorganic-based laser lift-off. Adv Mater 26:7480–7487. https://doi.org/10.1002/adma.201402472
- Liu Y, Wu L, Liu Q, Liu L, Ke S, Peng Z, Shi T, Yuan X, Huang H, Li J, Ye C, Chu PK, Wang J, Yu XF (2021) Topochemical synthesis of copper phosphide nanoribbons for flexible optoelectronic memristors. Adv Funct Mater 2110900:1–8. https://doi.org/10.1002/adfm.202110900

**Publisher's Note** Springer Nature remains neutral with regard to jurisdictional claims in published maps and institutional affiliations.

Springer Nature or its licensor (e.g. a society or other partner) holds exclusive rights to this article under a publishing agreement with the author(s) or other rightsholder(s); author self-archiving of the accepted manuscript version of this article is solely governed by the terms of such publishing agreement and applicable law.

